

QUANTUM MECHANICS

Two-particle quantum interference in tunnel-coupled optical tweezers

A. M. Kaufman,^{1,2} B. J. Lester,^{1,2} C. M. Reynolds,^{1,2} M. L. Wall,^{1,2} M. Foss-Feig,³
K. R. A. Hazzard,^{1,2} A. M. Rey,^{1,2} C. A. Regal^{1,2*}

The quantum statistics of atoms is typically observed in the behavior of an ensemble via macroscopic observables. However, quantum statistics modifies the behavior of even two particles. Here, we demonstrate near-complete control over all the internal and external degrees of freedom of two laser-cooled ⁸⁷Rb atoms trapped in two optical tweezers. This controllability allows us to observe signatures of indistinguishability via two-particle interference. Our work establishes laser-cooled atoms in optical tweezers as a promising route to bottom-up engineering of scalable, low-entropy quantum systems.

Quantum interference between possible detection paths for two indistinguishable particles yields information about quantum statistics and correlations (1, 2). An example is the Hong-Ou-Mandel (HOM) effect, which reveals bosonic quantum statistics through a coalescence effect that causes two indistinguishable photons incident on different ports of a beam splitter to emerge on the same, yet random, output port (3). The HOM effect has been observed with photons (3–5) and in an analogous experiment with electrons (6).

Here, we observe two-particle interference akin to the HOM effect with independently prepared bosonic atoms in tunnel-coupled optical tweezers (Fig. 1A). We control the single-atom quantum state by laser cooling each atom to its motional ground state and then directly observe the effects of their quantum indistinguishability. Whereas the role of quantum statistics in macroscopic ensembles of fermionic and bosonic atoms can be observed with Hanbury Brown and Twiss interference experiments (7–13), our system allows the study of nonclassical few-atom states with single-atom control.

Our results depend on the mobility of two wavelength-scale optical tweezers and single-site imaging, which are realized using the apparatus illustrated in Fig. 1B (14–16). For laser cooling ⁸⁷Rb atoms to the three-dimensional (3D) ground state (Fig. 1C) (16, 17) and imaging in position-resolved potentials, our tweezers are positioned far apart compared to the focused spot radius of 710 nm. For tunneling, the tweezers are brought close together such that there is a small, tunable overlap of the single-particle wave functions. Our full experimental sequence consists of the following steps: We image the initial atom positions, laser cool with Raman sideband cooling, perform tunneling experiments, and then image the atoms again. Hence, we can fol-

low the quantum dynamics between initial and final states that are both known with single-site resolution.

In Fig. 2, A to C, we study the single-atom tunneling dynamics by only considering experiments that, after stochastic loading (14), yield a single atom in the left or right well in the first image (fig. S1). After imaging and cooling, the atom is in the 3D motional ground state and the $|F = 2, m_F = 2\rangle \equiv |\uparrow\rangle$ spin state, where F and m_F are the total angular momentum quantum number and its projection along a quantization axis, respectively. The tweezer depths and spacing (Fig. 2A) are then decreased rapidly (slowly) with respect to the tunnel coupling (trap frequency) to prepare an initial state ideally localized in the left or right well (fig. S2). The tunnel coupling is given by $J = -\langle R|H_{\text{sp}}|L\rangle/\hbar$, where $|L\rangle$ ($|R\rangle$) is the lowest-energy, localized state in the left (right) well, and H_{sp} is the single-particle Hamiltonian (18). We control the double-well energy bias by varying the relative intensity of each tweezer. On the tunneling resonance, an atom prepared in the left well undergoes the coherent dynamics $|L\rangle \rightarrow \cos(Jt)|L\rangle + i\sin(Jt)|R\rangle$ (19–22). After an evolution time t in the presence of tunneling, the depth of the traps is rapidly increased to freeze the atom distribution, the traps are pulled apart, and the single-atom location is imaged.

Figure 2B demonstrates resonant coherent tunneling as measured by recording the likelihood of observing the atom in the left well (P_L) as a function of time for an atom starting in the left well (blue) or the right well (red). The tunneling can be tuned by varying either the tweezer spacing or the overall potential depth (fig. S3C). In Fig. 2B, a fit to the data reveals $J/2\pi = 262(4)$ Hz; Fig. 2C shows data in which J is increased to 348(4) Hz. One contribution to the subunity oscillation contrast is atom loss due to background collisions; in the duration of our experiments, the loss probability (P_{loss}) ranges from 0.03 to 0.05 and is known precisely for each experiment (fig. S1, table S1, and Fig. 2, B and C, gray regions). We also observe damping of the tunneling oscillations and finite initial contrast that is not accounted for by particle loss ($\tau \approx 10$ ms for $J/2\pi = 262$ Hz) (fig. S3B). These effects are most likely due to

experimental fluctuations of the double-well bias, and we experimentally find that the contrast and damping improve with increasing J (18).

We now consider the theoretical expectation for an equivalent dynamical experiment starting with two particles, one per well. For perfect cooling and spin preparation of the isolated atoms, the particles will be indistinguishable—that is, all degrees of freedom besides their position (left or right) will have been made the same. We know there is a particle in the left well and there is a particle in the right well, but we cannot associate any additional label to the particles. The bosonic atoms will then, necessarily, occupy the spatially symmetric state $|S\rangle \equiv \frac{1}{\sqrt{2}}(|L\rangle_1|R\rangle_2 + |R\rangle_1|L\rangle_2)$, where the ket subscript is a particle label. For poor cooling or spin preparation, the atoms can be distinguished by a degree of freedom other than their position; hence, the atoms can antisymmetrize in the additional degree of freedom and, in turn, have a projection onto the antisymmetric spatial state $|A\rangle \equiv \frac{1}{\sqrt{2}}(|L\rangle_1|R\rangle_2 - |R\rangle_1|L\rangle_2)$. The bosonic state can then be written as a mixture of the states $|\psi_{\pm}\rangle = \frac{1}{\sqrt{2}}(|S\rangle|\chi_{\pm}\rangle \pm |A\rangle|\bar{\chi}_{\pm}\rangle)$, where $|\chi_{\pm}\rangle = \frac{1}{\sqrt{2}}(|\chi\rangle_1|\bar{\chi}\rangle_2 \pm |\bar{\chi}\rangle_1|\chi\rangle_2)$ and $\{\chi, \bar{\chi}\}$ describe the other degree of freedom such as motional state $\{n, n'\}$ or spin $\{\uparrow, \downarrow\}$. Two atoms in either of the $|\psi_{\pm}\rangle$ states are distinguishable because the additional degree of freedom $\{\chi, \bar{\chi}\}$ is uniquely correlated with the atoms' positions: For the $|\psi_{+}\rangle$ ($|\psi_{-}\rangle$) state, the atom on the left is in state $|\chi\rangle$ ($|\bar{\chi}\rangle$) and the atom on the right is in state $|\bar{\chi}\rangle$ ($|\chi\rangle$). The ability to measure indistinguishability arises from the different dynamics exhibited in the symmetric and antisymmetric cases. The symmetric spatial state dynamically evolves as $|S\rangle \rightarrow |S\rangle\cos(2Jt) + \frac{i}{\sqrt{2}}(|L\rangle_1|L\rangle_2 + |R\rangle_1|R\rangle_2)\sin(2Jt)$. The antisymmetric state $|A\rangle$ undergoes destructive interference that prevents the two atoms from being in the same well, and hence displays no tunneling dynamics.

In Fig. 2D, we show the ideal dynamics for the distinguishable (purple), symmetric (black), and antisymmetric (brown) cases. We consider the observable $P_{11}(t)$, which is the likelihood to measure the atoms in separate wells as a function of t and is analogous to looking at coincidence counts on a pair of photon detectors. The symmetric $|S\rangle$ state yields unity contrast oscillations of $P_{11}(t)$, whereas $|A\rangle$ yields a time-independent $P_{11}(t) = 1$. Hence, the distinguishable states $|\psi_{\pm}\rangle$ result in a $P_{11}(t)$ that is the average of these dynamics and, as such, does not attain a value below 0.5. The tunneling between the wells yields an effective atom beam splitter where t varies the reflection and transmission coefficients. Of particular importance are the times $t_b \equiv 2\pi/8J$ and odd-integer multiples thereof (green dashed lines). At $t = t_b$, the tunneling splits each atom equally between the wells and thereby realizes a balanced atom beam splitter according to the transformations $|L\rangle \rightarrow \frac{1}{\sqrt{2}}(|L\rangle + i|R\rangle)$ and $|R\rangle \rightarrow \frac{1}{\sqrt{2}}(|R\rangle + i|L\rangle)$. Accordingly, for the $|S\rangle$ state, $P_{11}(t_b)$ vanishes in analogy to the indistinguishable photons incident on separate ports of a balanced beam splitter in the original HOM experiment (3). However, distinguishable atoms, like distinguishable photons, will yield $P_{11} = 0.5$ when equally beam split.

¹JILA, National Institute of Standards and Technology and University of Colorado, Boulder, CO 80309, USA.

²Department of Physics, University of Colorado, Boulder, CO 80309, USA. ³Joint Quantum Institute and the National Institute of Standards and Technology, Gaithersburg, MD 20899, USA.

*Corresponding author. E-mail: regal@colorado.edu

In Fig. 2E, we experimentally investigate the population dynamics observed with two particles. We plot $P_{11}(t)$ for cases in which the stochastic loading results in two atoms, one in each well (black squares); these points are taken in the same experimental sequence as the single-particle data in Fig. 2B. In our atom detection protocol, we image scattered light from the two well-separated traps onto a charge-coupled device (CCD) array. During the 25- to 50-ms imaging time, the atoms are cooled by polarization gradient cooling, during which light-assisted atomic collisions result in a signal corresponding to either zero or one atom (14, 22, 23). P_{11} is determined by the distinct signature in which the image indicates one atom in each well. If the experiment yields two atoms in one well, P_{20} or P_{02} , this is manifest by final images that yield zero atoms, or in some cases one atom in a single well (fig. S1) (18). To accurately interpret P_{11} , we take into account signal depletion caused by the single-particle loss described earlier (P_{loss}). This effect reduces the maximum value that can be achieved by the measured P_{11} to $(1 - P_{\text{loss}})^2$.

In analyzing the results of the two-particle dynamics, our goal is to compare $P_{11}(t)$ from our two-particle measurement to that of a theoretical expectation for uncorrelated, distinguishable atoms, which we refer to as $P_{\text{dist}}(t)$. P_{dist} at any time can be calculated directly from corresponding single-particle data via $P_{\text{dist}} = P_L^1 P_R^2 + P_R^1 P_L^2$ (purple circles in Fig. 2E) (18). Here, $P_L^{1(2)}$ corresponds to measuring an atom in the left (right) well when an atom starts in the left (right) well, i.e., the blue (red) data of Fig. 2B, and $P_R^{1(2)}$ is the corresponding information for measuring an atom in the right well. A calculation of P_{dist} directly from the single-particle points inherently contains both loss and finite single-particle contrast. For example, $P_{\text{dist}}(t_b)$ reaches a minimum value consistent with $(1 - P_{\text{loss}})^2/2 \approx 0.5 - P_{\text{loss}}$, and the amplitude of $P_{\text{dist}}(t)$ is consistent with the expectation of one-half the product of the single-particle contrasts (18). We can compare the amplitude of oscillation for the distinguishable expectation (purple circles) to our two-particle measurement (black squares). We find that these

values differ by 6σ (18): $A_{P_{\text{dist}}} = 0.282(12)$ and $A_{P_{11}} = 0.46(2)$.

A full treatment of the observed $P_{11}(t)$ must also consider potential effects of interactions between the atoms. In many experiments with atoms in optical lattices, the on-site interaction energy U is the dominant scale (19, 24); however, we intentionally operate in a regime where U is smaller than J . For the data shown in Fig. 2E, $U = 0.44(4)J$ (18). In Fig. 2F, we demonstrate two-particle oscillations for experimental conditions of an even smaller relative interaction $U = 0.22(2)J$, with measurements $A_{P_{11}} = 0.48(2)$ and $A_{P_{\text{dist}}} = 0.306(18)$. The similarity of these results to those in Fig. 2E suggests that interactions are not a relevant scale in either experiment. A careful theoretical analysis also demonstrates that existing interactions between distinguishable atoms could not mimic the observed signal of two-particle interference (18) (figs. S5 and S6).

We now study the behavior at the balanced tunneling point t_b , where, in analogy to HOM experiments, the two-particle interference is most readily observed. Using multiple experimental knobs, we can vary the indistinguishability of the atoms and observe a variation in $P_{11}(t_b) = P_b$. We start by studying the dependence of P_b on the relative spin state of the two atoms using two distinct methods. In the first method, after cooling the atoms, we apply a variable-length microwave pulse that couples the $|\uparrow\rangle$ and $|\downarrow\rangle$ spin states in only the right well (fig. S4). This is accomplished by shifting the transition in the left well out of resonance using a circularly polarized, tightly focused laser spot (18). Upon π rotation of the right spin, the atoms become distinguishable, and we expect the two-particle interference dip of P_{11} below P_{dist} to disappear. The observed dependence on the microwave pulse area is shown in Fig. 3A; for comparison, we show that P_{dist} (purple circles), calculated from the single-particle measurements, remains constant and near $(1 - P_{\text{loss}})^2/2$. We study multiple spin rotations to show that the interference is recovered after a 2π rotation. We find that the frequency of oscillation is $32.6(6)$ kHz, which is in agreement with the measured microwave Rabi frequency of $32.05(18)$ kHz. The displayed fit to the data determines $P_b^{\text{min}} = 0.314(14)$, and the amplitude of the variation in P_b is $0.15(2)$. Taking into account the spin rotation fidelity, we expect an amplitude of $0.84((1 - P_{\text{loss}})^2/2 - P_b^{\text{min}}) = 0.130(13)$ (18), which is consistent with the measured value. The agreement further substantiates the irrelevance of interactions, which are nearly constant as the two-particle spin state is varied (25), and hence not responsible for the observed variation in P_b .

In the second spin study, we couple the $|\uparrow\rangle$ and $|\downarrow\rangle$ spin states of atoms in both wells using a pair of Raman beams. This global rotation avoids any systematic effects that might be introduced by single-site addressing. During the time (25 ms) between the Raman pulse and the tunneling, the atoms lose their spin coherence, and hence the spin state of each atom is in an incoherent mixture. Ideally, odd-integer multiples of a $\pi/2$ -pulse yield an equal mixture of all possible two-atom

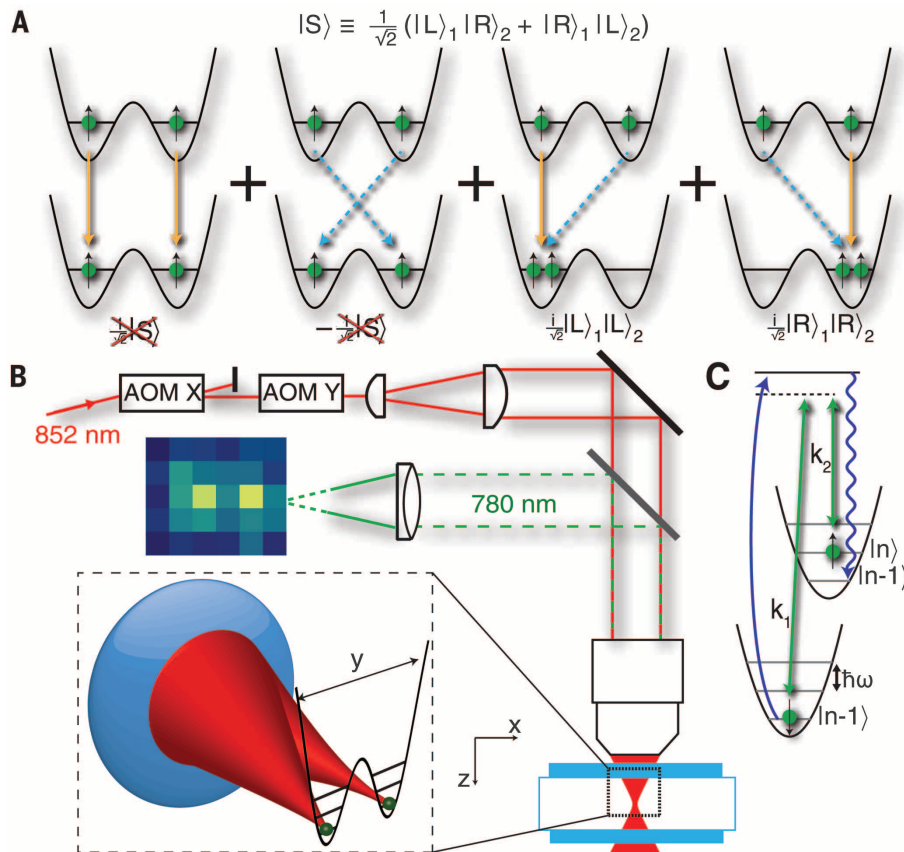


Fig. 1. Quantum interference of two particles. (A) The initial two-particle state is a ground state spin-up atom in each optical tweezer, denoted by $|S\rangle \equiv \frac{1}{\sqrt{2}} (|L\rangle_1 |R\rangle_2 + |R\rangle_1 |L\rangle_2)$, where the ket subscript is a particle label, and the single-particle states $|L\rangle$ ($|R\rangle$) correspond to an atom localized in the left (right) well. For a tunneling time that realizes a balanced atom beam splitter, destructive interference yields the state $\frac{i}{\sqrt{2}} (|L\rangle_1 |L\rangle_2 + |R\rangle_1 |R\rangle_2)$. (B) Experimental setup. The apparatus for realizing tunneling between optical tweezers uses high numerical aperture optics combined with control of the tweezers' positions and depths with acousto-optic modulators (AOMs). The same objective that creates the focused tweezer potentials also collects 780 nm fluorescence from the optically trapped atoms. (C) The sideband cooling is accomplished with lasers driving coherent (green) and spontaneous (blue) Raman transitions that couple to the atomic motion and spin states $|F = 1, m_F = 1\rangle \equiv |\uparrow\rangle$ and $|F = 2, m_F = 2\rangle \equiv |\downarrow\rangle$.

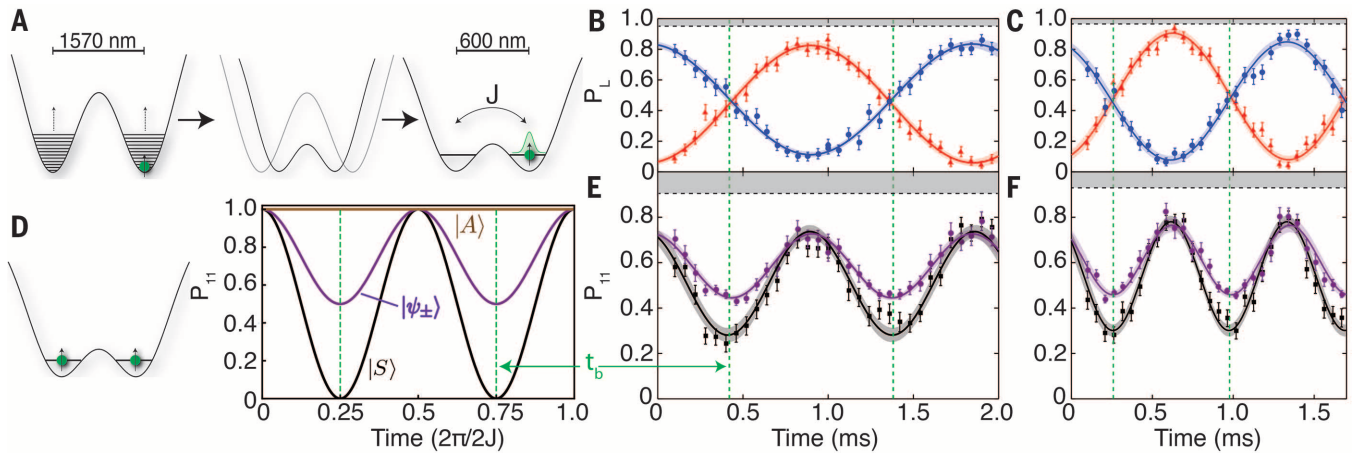


Fig. 2. Single- and two-particle tunneling. (A) While the tweezers are 23(1) MHz deep, the atom is imaged, cooled and optically pumped to $|\uparrow\rangle$. For tunneling experiments, the tweezers are swept together such that the two Gaussian functions (double-well minima) are centered ≈ 800 nm (≈ 600 nm) apart, and the total trap intensity is decreased to a single-well depth of either 96 kHz or 60 kHz. (B) Resonant tunneling oscillations at $2J$ for an 808-nm Gaussian function spacing and a 96-kHz depth. Blue circles (red triangles) are the expectation value $P_L^{(2)}$ for finding an atom in the left (right) well given an initial single atom in the left (right) well. The gray shaded region indicates atom loss P_{loss} . (C) Same as B except with an 805-nm Gaussian function spacing and a depth of 60 kHz. (D) Ideal $P_{11}(t)$ for two-particle tunneling

dynamics initiated at $t = 0$ and in the symmetric state $|S\rangle$, the distinguishable states $|\psi_{\pm}\rangle$, and the antisymmetric state $|A\rangle$. The dashed green lines correspond to t_b . (E) Measured two-particle dynamics during the same experimental sequence as in (B). Likelihood to measure exactly one atom in each well (P_{11}) for the initial condition of an atom prepared in each well (black squares). Distinguishable expectation P_{dist} calculated from the single-particle data in (B) (purple circles). The gray shaded region above the dashed black line indicates the expected reduction from atom loss. (F) Same as (E) except with a larger value of J/U using the double-well parameters of (C). In all plots, the shaded regions are the 95% confidence interval for a sinusoidal fit. The error bars are the standard error in the measurement; each black (red or blue) data point is the mean of ≈ 140 (100) atom measurements.

spin states, and hence the two-particle interference dip should be reduced by $1/2$. As a function of Raman pulse area (Fig. 3B), the frequency of oscillation is 65.5 ± 1.2 kHz, which, as expected, is twice the measured Raman Rabi frequency of $32.3(3)$ kHz. The displayed fit to the data determines $P_b^{\text{min}} = 0.296(10)$, and the amplitude of the variation in P_b is $0.085(15)$. Taking into account the relative spin rotation fidelity of $0.90(3)$, we expect an amplitude of $(0.90^2/2)[(1 - P_{\text{loss}})^2/2 - P_b^{\text{min}}] = 0.069(6)$, which is consistent with the measured amplitude.

Last, we study the dependence of P_b on the motional state of the atoms in Fig. 3C. During the last stage of cooling, we vary the frequency δ_{Cool} of one Raman beam that controls the cooling along the weak axis (z) of both tweezer wells. For a separable potential, motional excitation along this axis would leave the single-particle tunneling unaffected. For our nonseparable tweezer potential, we expect and observe some variation in the tunneling (18), but near t_b the single-particle tunneling still results in a relatively constant P_{dist} (purple circles), which is consistent with the distinguishable expectation $(1 - P_{\text{loss}})^2/2 = 0.4660(14)$. For the two-particle measurements, at the primary sideband cooling resonance ($\delta_{\text{Cool}} = 0$), we observe a dip to $P_b^{\text{min}} = 0.28(2)$, which is a value below the distinguishable expectation.

In all of our measurements, the value of P_b^{min} is observed to be finite, and it is useful to consider the origin of imperfections that could lead to the observed value. If residual atom temperature along the weak z axis were the only contributing factor, the central value of our single-atom ground-state fraction [measured by sideband spectroscopy to

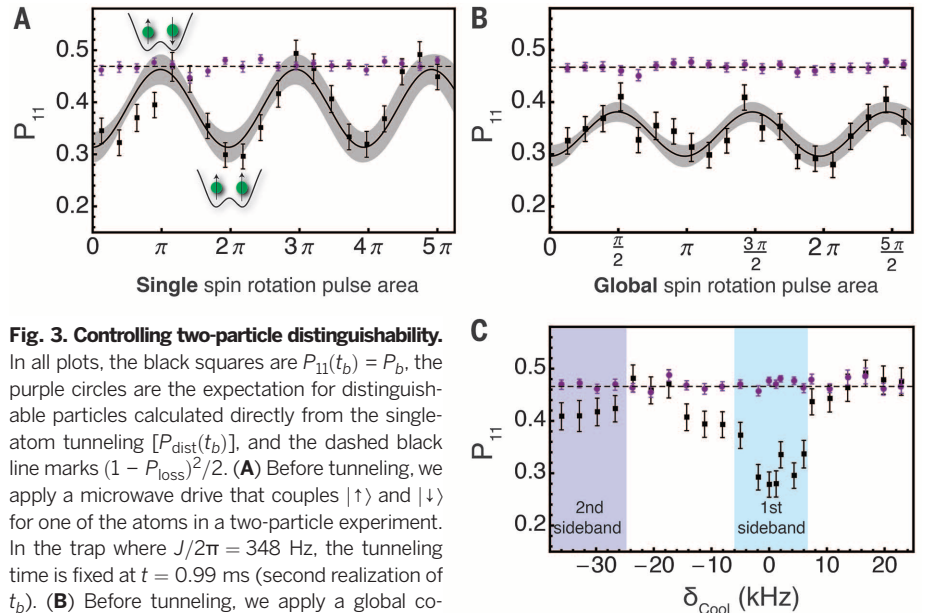


Fig. 3. Controlling two-particle distinguishability.

In all plots, the black squares are $P_{11}(t_b) = P_b$, the purple circles are the expectation for distinguishable particles calculated directly from the single-atom tunneling [$P_{\text{dist}}(t_b)$], and the dashed black line marks $(1 - P_{\text{loss}})^2/2$. (A) Before tunneling, we apply a microwave drive that couples $|\uparrow\rangle$ and $|\downarrow\rangle$ for one of the atoms in a two-particle experiment. In the trap where $J/2\pi = 348$ Hz, the tunneling time is fixed at $t = 0.99$ ms (second realization of t_b). (B) Before tunneling, we apply a global coherent drive of varied pulse area to couple $|\uparrow\rangle$ and $|\downarrow\rangle$ and then allow for decoherence. In the trap where $J/2\pi = 262$ Hz, the tunneling time is fixed at $t = 0.45$ ms. In (A) and (B), the solid line and shaded band are sinusoidal fits and the associated 95% confidence interval. (C) We vary the detuning (δ_{Cool}) of the cooling beams of motion along the z axis. In the trap where $J/2\pi = 262$ Hz, the tunneling time is fixed at $t = 0.45$ ms. The two shaded regions correspond to frequency ranges of efficient (1st sideband) and less efficient (2nd sideband) cooling. For all plots, each black data point is the average of ≈ 360 measurements, and each set of measurements corresponding to a purple point is the average of ≈ 240 measurements. All error bars are the standard error in the measurement.

be 85% [$16, 18$] would correspond to $P_b^{\text{min}} = 0.12$. Hence, it is likely that the finite P_b^{min} is further enlarged by technical fluctuations similar to those that lead to our finite single-particle contrast.

We have demonstrated an experimental system with which we achieve quantum control over the motion, position, and spin of single neutral atoms. Through a two-particle interference experiment,

we have shown that it is possible to create a low-entropy bosonic state by individually placing atoms in their motional ground state with laser cooling (26–28). Our results lay a foundation for linear quantum computing with atoms (29), interferometric highly sensitive force detection (30), control of neutral atoms in nanoscale optical devices (31, 32), and quantum simulation with laser-cooled atoms in scalable optical tweezer arrays.

REFERENCES AND NOTES

- R. J. Glauber, *Phys. Rev.* **130**, 2529–2539 (1963).
- R. Hanbury Brown, R. Q. Twiss, *Nature* **177**, 27 (1956).
- C. K. Hong, Z. Y. Ou, L. Mandel, *Phys. Rev. Lett.* **59**, 2044–2046 (1987).
- J. Beugnon *et al.*, *Nature* **440**, 779–782 (2006).
- C. Lang *et al.*, *Nat. Phys.* **9**, 345–348 (2013).
- E. Bocquillon *et al.*, *Science* **339**, 1054–1057 (2013).
- M. Yasuda, F. Shimizu, *Phys. Rev. Lett.* **77**, 3090–3093 (1996).
- S. Fölling *et al.*, *Nature* **434**, 481–484 (2005).
- M. Schellekens *et al.*, *Science* **310**, 648–651 (2005).
- A. Öttl, S. Ritter, M. Köhl, T. Esslinger, *Phys. Rev. Lett.* **95**, 090404 (2005).
- T. Rom *et al.*, *Nature* **444**, 733–736 (2006).
- T. Jeltes *et al.*, *Nature* **445**, 402–405 (2007).
- S. S. Hodgman, R. G. Dall, A. G. Manning, K. G. H. Baldwin, A. G. Truscott, *Science* **331**, 1046–1049 (2011).
- N. Schlosser, G. Reymond, I. Protchenko, P. Grangier, *Nature* **411**, 1024–1027 (2001).
- F. Serwane *et al.*, *Science* **332**, 336–338 (2011).
- A. M. Kaufman, B. J. Lester, C. A. Regal, *Phys. Rev. X* **2**, 041014 (2012).
- C. Monroe *et al.*, *Phys. Rev. Lett.* **75**, 4011–4014 (1995).
- Materials and methods are available as supplementary materials on Science Online.
- S. Fölling *et al.*, *Nature* **448**, 1029–1032 (2007).
- M. Anderlini *et al.*, *Nature* **448**, 452–456 (2007).
- J. Sebby-Strabley *et al.*, *Phys. Rev. Lett.* **98**, 200405 (2007).
- C. Weitenberg *et al.*, *Nature* **471**, 319–324 (2011).
- W. S. Bakr, J. I. Gillen, A. Peng, S. Fölling, M. Greiner, *Nature* **462**, 74–77 (2009).
- R. Ma *et al.*, *Phys. Rev. Lett.* **107**, 095301 (2011).
- M. Egorov *et al.*, *Phys. Rev. A* **87**, 053614 (2013).
- V. Vuletić, C. Chin, A. J. Kerman, S. Chu, *Phys. Rev. Lett.* **81**, 5768–5771 (1998).
- D. S. Weiss *et al.*, *Phys. Rev. A* **70**, 040302 (2004).
- A. Steffen *et al.*, *Proc. Natl. Acad. Sci. U.S.A.* **109**, 9770–9774 (2012).
- P. Kok, K. Nemoto, T. C. Ralph, J. P. Dowling, G. J. Milburn, *Rev. Mod. Phys.* **79**, 135–174 (2007).
- V. Giovannetti, S. Lloyd, L. Maccone, *Science* **306**, 1330–1336 (2004).
- E. Vetsch *et al.*, *Phys. Rev. Lett.* **104**, 203603 (2010).
- J. D. Thompson *et al.*, *Science* **340**, 1202–1205 (2013).

ACKNOWLEDGMENTS

We thank T. P. Purdy for useful discussions. This work was supported by the David and Lucile Packard Foundation and the National Science Foundation (NSF) under grant no. 1125844. C.A.R. acknowledges support from the Clare Boothe Luce Foundation, A.M.K. and C.M.R. from the National Defense Science and Engineering Graduate Fellowships, and B.J.L. from the NSF Graduate Research Fellowship Program. K.R.A.H., M.L.W., and A.M.R. acknowledge funding from NSF-Physics at the Information Frontier, Army Research Office and Air Force Office of Scientific Research. K.R.A.H. and M.F.-F. acknowledge support from a National Research Council postdoctoral fellowship.

SUPPLEMENTARY MATERIALS

www.sciencemag.org/content/345/6194/306/suppl/DC1
Materials and Methods

Figs. S1 to S6

Table S1

References (33–36)

22 December 2013; accepted 6 June 2014

Published online 26 June 2014;

10.1126/science.1250057

OPTICAL METROLOGY

Electro-optical frequency division and stable microwave synthesis

Jiang Li,^{1*} Xu Yi,^{1*} Hansuek Lee,¹ Scott A. Diddams,² Kerry J. Vahala^{1†}

Optical frequency division by using frequency combs has revolutionized time keeping and the generation of stable microwave signals. We demonstrate optical frequency division and microwave generation by using a tunable electrical oscillator to create dual combs through phase modulation of two optical signals that have a stable difference frequency. Phase-locked control of the electrical oscillator by means of optical frequency division produces stable microwaves. Our approach transposes the oscillator and frequency reference of a conventional microwave frequency synthesizer. In this way, the oscillator experiences large phase noise reduction relative to the frequency reference. The electro-optical approach additionally relaxes the need for highly linear photodetection of the comb mode spacing. As well as simplicity, the technique is also tunable and scalable to higher division ratios.

The photomixing of two highly coherent laser signals is a well-known approach to generate a stable radio frequency (RF) or microwave signal (1, 2). Recently, however, a different approach to all-optical signal generation has been demonstrated that may revolutionize applications that require high-stability microwaves. Rather than photomixing stabilized laser signals to directly produce a microwave signal, the approach uses an octave-spanning, self-referenced frequency comb to divide a stable optical reference frequency down to microwave or RF rates (3). Frequency dividers are widely used in electronics to generate new frequencies from a single base oscillator or to coherently link different frequency bands. As an ancillary benefit, all frequency dividers reduce the phase noise spectral density of the output signal relative to the input by the square of the division ratio. The new optical frequency dividers perform division by a factor of ~50,000 (the ratio of optical to microwave frequencies), so that phase-noise reduction is greater than 10⁹. Moreover, reference-cavity stabilized lasers exhibit a superior, fractional frequency stability in comparison with electrical oscillators (4, 5). Optical dividers applied to such signals thereby generate microwave signals with an exceedingly low phase noise level (3).

We present a way to generate high-performance microwave signals through optical frequency division (OFD) by using a cascade of direct phase modulation and self-phase modulation to create an optical comb (6–9). Because the spectral line spacing is set by the electrical oscillator used to drive the phase modulators (as opposed to an optical resonator), the method of microwave synthesis has similarities to conventional microwave synthesizers while also leveraging the power of OFD so as to reduce phase noise.

In our approach, two laser lines having good relative frequency stability provide an optical re-

ference for the microwave source (Fig. 1A). These laser lines are produced by Brillouin oscillation in a single high-quality-factor (Q) microcavity. However, the lines could also result from any stable optical references, including various types of dual-mode lasers (10–15), two lasers locked to distinct optical modes of a reference cavity (16), or lasers stabilized to atomic transitions (17). The laser lines enter the frequency divider portion of the signal generator, where they are phase-modulated by a pair of modulators at a frequency set by a voltage-controlled electrical oscillator (VCO). The sideband spectrum created by the phase modulators is further broadened through pulse-forming and self-phase modulation in an optical fiber (8, 18, 19). The comb of lines extending from each laser line results in a pair of sidebands near the midpoint of the frequency span. These are optically filtered and detected. The detected beat-note signal contains the phase noise of the VCO, but magnified by the optical division factor. It therefore provides a suitable error signal for phase-lock loop control of the VCO.

We contrast this microwave source that is based on electro-optical frequency division (EOFD) with a conventional microwave source that is based on electrical frequency division of a VCO (20). In the conventional approach (Fig. 1B), the VCO provides the highest frequency in the system. It is stabilized through electrical frequency division and phase comparison with a lower-frequency reference oscillator, such as a quartz oscillator. A consequence is that the stabilized VCO has a phase noise level that is always higher than the reference oscillator phase noise by the square of their frequency ratio (the frequency division ratio). In contrast, our optical version reverses the positions of the reference and the VCO in the frequency domain. Specifically, the reference is provided by the frequency difference of the laser lines, and this frequency difference is made much greater than the frequency of the VCO (in the present implementation, this is a nondetectable rate set at ~150 times the VCO frequency). Moreover, this reference frequency is divided down to the VCO frequency, as opposed to dividing the VCO frequency down to

¹T. J. Watson Laboratory of Applied Physics, California Institute of Technology, Pasadena, CA 91125, USA. ²Time and Frequency Division, National Institute of Standards and Technology, Boulder, CO 80305, USA.

*These authors contributed equally to this work. †Corresponding author. E-mail: vahala@caltech.edu

This copy is for your personal, non-commercial use only.

If you wish to distribute this article to others, you can order high-quality copies for your colleagues, clients, or customers by [clicking here](#).

Permission to republish or repurpose articles or portions of articles can be obtained by following the guidelines [here](#).

The following resources related to this article are available online at www.sciencemag.org (this information is current as of March 15, 2015):

Updated information and services, including high-resolution figures, can be found in the online version of this article at:

<http://www.sciencemag.org/content/345/6194/306.full.html>

Supporting Online Material can be found at:

<http://www.sciencemag.org/content/suppl/2014/06/25/science.1250057.DC1.html>

A list of selected additional articles on the Science Web sites **related to this article** can be found at:

<http://www.sciencemag.org/content/345/6194/306.full.html#related>

This article **cites 35 articles**, 7 of which can be accessed free:

<http://www.sciencemag.org/content/345/6194/306.full.html#ref-list-1>

This article has been **cited by** 3 articles hosted by HighWire Press; see:

<http://www.sciencemag.org/content/345/6194/306.full.html#related-urls>

This article appears in the following **subject collections**:

Physics

<http://www.sciencemag.org/cgi/collection/physics>